Imaging tissues for biomedical research using the high-resolution micro-tomography system nanotom® m

Hans Deyhle[a], Georg Schulz[a], Anna Khimchenko[a], Christos Bikis[a], Simone E. Hieber[a], Claude Jaquiery[b], Christoph Kunz[b], Magdalena Müller-Gerbl[c], Sebastian Höchel[c], Till Saxer[d], Anja K. Stalder[a], Bernd Ilgenstein[a], Felix Beckmann[e], Peter Thalmann[a], Marzia Buscema[a], Nadja Rohr[f], Margaret N. Holme[a,g], and Bert Müller[a]

[a]Biomaterials Science Center, Department of Biomedical Engineering, University of Basel, 4123 Allschwil, Switzerland
[b]Cranio-Maxillofacial Surgery, University Hospital Basel, 4031 Basel, Switzerland
[c]Department of Biomedicine, Musculoskeletal Research, University of Basel, 4056 Basel, Switzerland
[d]Cardiology Division, University Hospitals of Geneva, 1206 Geneva, Switzerland
[e]Institute of Materials Research, Helmholtz-Zentrum Geesthacht, 21502 Geesthacht, Germany
[f]Division for Materials Science and Engineering, Clinic for Reconstructive Dentistry and Temporomandibular Disorders, University Hospital of Dental Medicine, 4056 Basel, Switzerland
[g]Department of Materials, Imperial College London, South Kensington Campus, London SW7 2BP, United Kingdom

ABSTRACT

Micro computed tomography (μCT) is well established in virtually all fields of biomedical research, allowing for the non-destructive volumetric visualization of tissue morphology. A variety of specimens can be investigated, ranging from soft to hard tissue to engineered structures like scaffolds. Similarly, the size of the objects of interest ranges from a fraction of a millimeter to several tens of centimeters. While synchrotron radiation-based μCT still offers unrivaled data quality, the ever-improving technology of cathodic tube-based machines offers a valuable and more accessible alternative. The Biomaterials Science Center of the University of Basel operates a nanotom® m (phoenix|x-ray, GE Sensing & Inspection Technologies GmbH, Wunstorf, Germany), with a 180 kV source and a minimal spot size of about 0.9 μm. Through the adjustable focus-specimen and focus-detector distances, the effective pixel size can be adjusted from below 500 nm to about 80 μm. On the high-resolution side, it is for example possible to visualize the tubular network in sub-millimeter thin dentin specimens. It is then possible to locally extract parameters such as tubule diameter, density, or alignment, giving information on cell movements during tooth formation. On the other side, with a horizontal shift of the 3,072 pixels × 2,400 pixels detector, specimens up to 35 cm in diameter can be scanned. It is possible, for example, to scan an entire human knee, albeit with inferior resolution. Lab source μCT machines are thus a powerful and flexible tool for the advancement of biomedical research, and a valuable and more accessible alternative to synchrotron radiation facilities.

Keywords: micro computed tomography, lab source, dentin tubules, coronary artery, osteogenic distraction, human cerebellum, bone graft, human knee

1. INTRODUCTION

Micro computed tomography (μCT) is well established in virtually all fields of biomedical research.[1–5] It allows for the non-destructive volumetric visualization of tissue morphology. Synchrotron radiation-based μCT offers unrivaled data quality both with respect to spatial resolution and contrast.[6,7] The high photon flux available

Further author information: (Send correspondence to H. D.)
H. D.: E-mail: hans.deyhle@unibas.ch, Telephone: +41 61 207 54 39

Developments in X-Ray Tomography X, edited by Stuart R. Stock, Bert Müller, Ge Wang, Proc. of SPIE Vol. 9967, 99670Q · © 2016 SPIE · CCC code: 0277-786X/16/$18 · doi: 10.1117/12.2237809

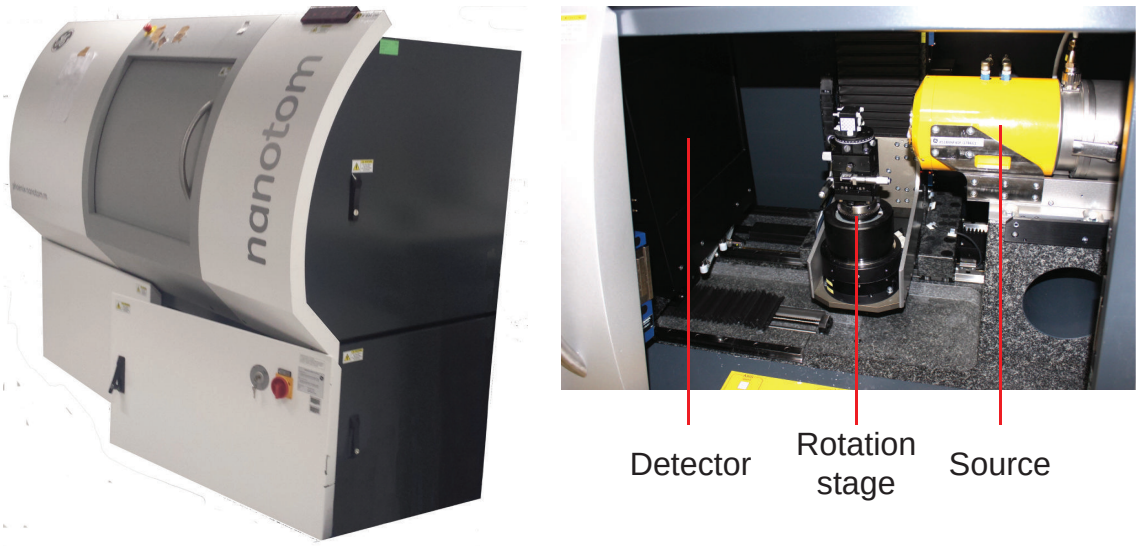

Figure 1. The nanotom® m is equipped with a 180 kV nanofocus transmission source. The source-detector distance can be adjusted from 225 to 600 mm, and the source-specimen distance from 1.8 to 400 mm, allowing for effective pixel sizes from 300 nm to 67 µm.

at these sources allows operating µCT measurements at selected photon energies. This, in return, allows for the quantitative determination of the local attenuation coefficients µ when measuring in absorption contrast. In addition, several approaches for phase retrieval exist,[8–10] and the ever-increasing coherence of the third-generation sources is driving the development of diffraction-limited imaging methods.[11–14]

Beamtime at synchrotron sources is, however, limited, thus making the acquisition of a statistically relevant number of specimens challenging if not impossible. Therefore, laboratory-based systems are of high interest for the biomedical community. Although the information obtained by cathode source scanners is not fully quantitative due to the polychromatic nature of the generated radiation, morphological information can nonetheless be obtained.[15] The Biomaterials Science Center of the University of Basel operates a nanotom® m (phoenix|x-ray, GE Sensing & Inspection Technologies GmbH, Wunstorf, Germany). The machine is highly flexible. It is equipped with a 180 kV source and reaches a minimal spot size of about 0.9 µm. Through the adjustable focus-specimen and focus-detector distances, the effective pixel size can be adjusted from below 600 nm to about 80 µm. It is thus suitable for the investigation of a variety of specimens of both low and high Z materials, while specimen size can range from several hundred micrometers to several centimeters. On the high-resolution side, it is for example possible to visualize the tubular network in sub-millimeter thin dentin specimens. It is then possible to locally extract parameters such as tubule diameter, density, or alignment, giving information on cell movements during tooth formation. On the other side, with a horizontal shift of the 3,072 pixels × 2,400 pixels detector, specimens up to 35 cm in diameter can be scanned. It is possible, for example, to scan an entire human knee, albeit with inferior resolution. This proceeding aims to give a partial overview over some of the research topics addressed within the framework of national and international partners.

2. METHODS

The data shown were all measured on the nanotom® m (phoenix|x-ray, GE Sensing & Inspection Technologies GmbH, Wunstorf, Germany) operated at the Biomaterials Science Center of the University of Basel (Allschwil, Switzerland), unless mentioned otherwise. The scanner is equipped with a 180 kVp/15 W transmission source. Two targets are available at the moment. The W target on diamond window is more suitable for acceleration voltages from 50 kV upwards, delivering a higher photon flux compared to the W target on a Be window, which

finds applications for very small or low absorbing specimens. The detection unit is a temperature stabilized GE DXR detector with 3072 pixels × 2400 pixels (14 bit depth, 100 µm pixel length). The source-detector distance can be adjusted from 225 to 600 mm, and the source-specimen distance from 1.8 to 400 mm, allowing for effective pixel sizes from 300 nm to 67 µm.

3. SPECIMENS

3.1 Human cerebellum

Histological sectioning is the gold standard for the inspection of soft tissue biopsies. The method offers high lateral spatial resolution sufficient for sub-cellular resolution as well as the possibility for functional staining. The drawback is that only information in two dimensions (2D) is obtained. It was shown that 2D information might result in imprecise measurements, for example resulting in the underestimation of inter-object distances within the specimen.[16] In addition, the obtained section might not be representative for the whole three-dimensional (3D) specimen.[17] To overcome these challenges, it is advantageous to extend histology to the third dimension by means of µCT.[1,18] Figures 2 (a) through (c) show µCT scans of a paraffin-embedded human cerebellum biopsy of a 73-year-old man at increasing magnifications. Written consent for scientific use was obtained. All procedures were conducted in accordance with the Declaration of Helsinki and approved by the Ethikkommission Nordwestschweiz. The data were acquired on the nanotom® m at an acceleration voltage of 60 kV and a beam current of 350 µA. 1900 projections with 3 s exposure time each were acquired over 360°. The effective voxel length corresponded to 3.5 µm. For comparison, Figures 2 (d) through (f) show the same slices, this time acquired with a grating interferometry (XGI) setup at the beamline ID19 at the European Synchrotron Radiation Facility (ESRF, Grenoble, France).[19] The mean energy of the pink beam was 19.45 keV. An Si phase grating G_1 with a period of $p_1 = 4.8$ µm and structure height $h_1 = 23$ µm and Au analyser grating G_2 with a period of $p_2 = 2.4$ µm and structure height $h_2 = 50$ µm were used. The distance between the two gratings was set to the eleventh fractional Talbot distance (465 mm). 1200 projections were acquired over 360°. For each projection, four images over one grating period were taken, with 2 s exposure time each. It is apparent that while the contrast of the XGI data is superior with respect to the attenuation data from the nanotom® m, the spatial resolution is at least comparable, if not superior in the attenuation data. For example, individual Purkinje cells are more readily distinguished in Fig. 2c compared to Fig. 2f. Figs 2g and h compare the µCT data and histology directly. While histology provides higher spatial resolution, the main features can be distinguished in both images. The line plot in Fig. 2i reinforces this notion.[1]

3.2 Stenosed human coronary arteries

Heart diseases are among the top causes of death worldwide:[20] Up to 50 % of people suffering a heart attack die before arriving at the hospital. Shear-stress sensitive liposomes[21,22] loaded with a vasodilator are a valid tool to overcome the high risk of mortality and to improve subsequent quality of life after the attack. The liposomes release their payload under increased shear stress as found in constricted coronary arteries. To assess the shear stresses present in constricted arteries, their morphology has to be known. µCT is ideally suited to determine lumen size in the healthy and diseased case.[23] Figures 3 a through c show three virtual orthogonal slices through the dataset of a paraffin-embedded stenosed human coronary artery. The data were acquired at 60 kV acceleration voltage and 310 µA beam current. 1000 projections over 360° were acquired. For each projection, three frames with 1.25 s exposure time each were averaged. The focus-specimen and focus-detector distances were adjusted to 40 mm and 225 mm, respectively, resulting in an effective voxel length of 17.8 µm. The calcified plaque is shown in yellow to blue, the vessel wall in light gray and paraffin in dark gray. Although the attenuation of the vessel wall is much lower compared to that of the plaque, it can be clearly distinguished from the embedding material.

3.3 Graft for bone augmentation

For the insertion of a dental implant, sufficient bone offer is required to ensure implant stability.[2,17] As bone retraction is often observed after the removal of a tooth, bone augmentation can be successfully applied to ensure the required bone offer for the successful insertion of dental implants. While transplantation of autologous bone remains the gold standard, in many patients suffering from critical bone volume reduction (pathological

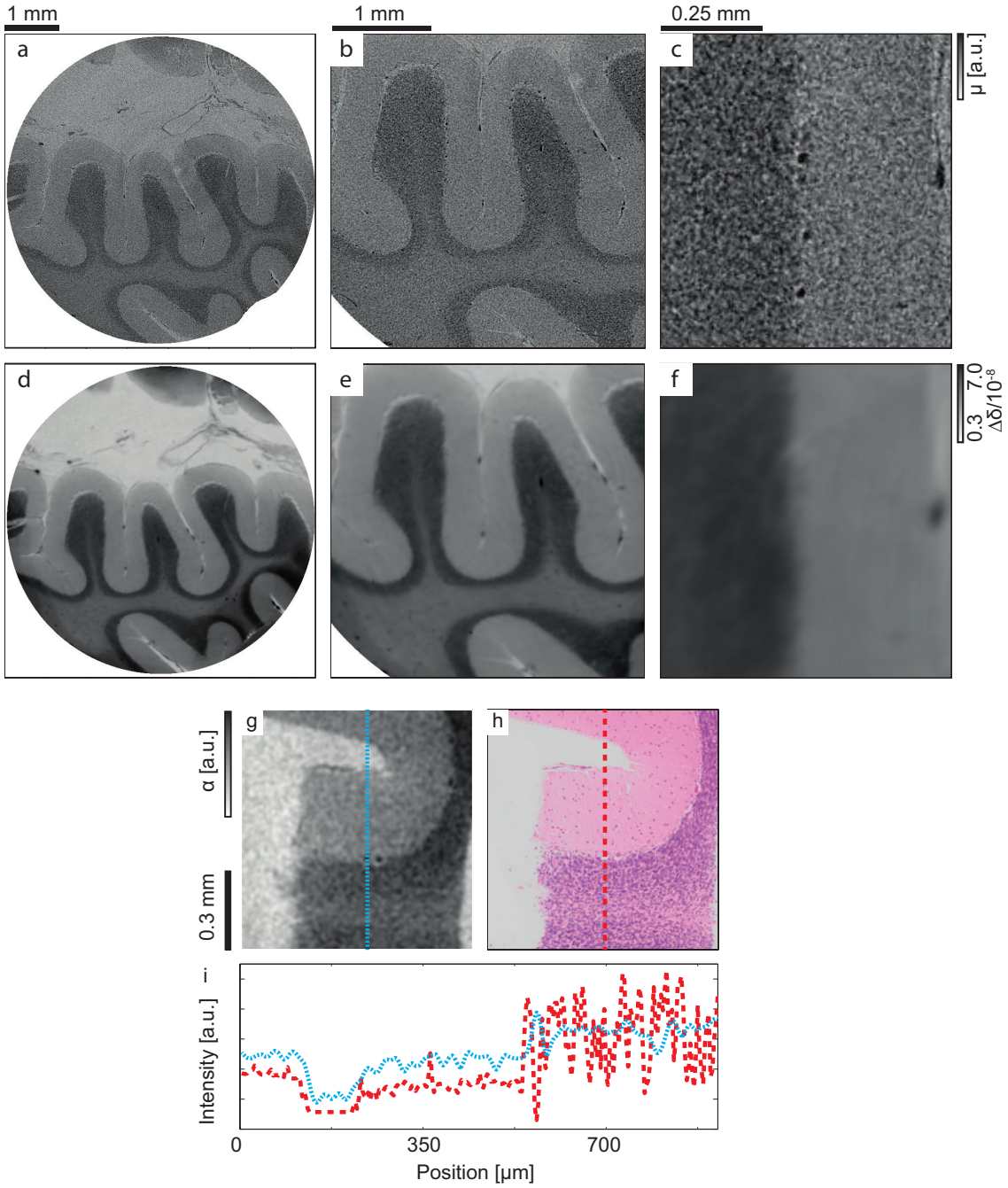

Figure 2. **(a)** Virtual cut through the dataset of a paraffin embedded human cerebellum, measured with the nanotom® m. *Stratum moleculare* surrounded by *stratum granulosum* can be identified. **(b)** Zoom-in of (a). **(c)** Zoom-in of (b). Individual Purkinje cells can be seen as dark spots between *stratum moleculare* (left) and *stratum granulosum* (right). **(d)** Same slice as (a) from a dataset acquired at the beamline ID19 (ESRF, Grenoble, France). Contrast is improved with respect to (a). **(e)** Zoom-in of (b), showing the same structures. **(f)** Zoom in of (e), showing the same region as in (c). It is apparent that while contrast is improved with respect to (c), spatial resolution is insufficient to resolve individual Purkinje cells. **(g,h)** Comparison of μCT data and histology. The lineplots in **(i)** show that the main features can be identified in both modalities. Histology however retains a higher level of detail.

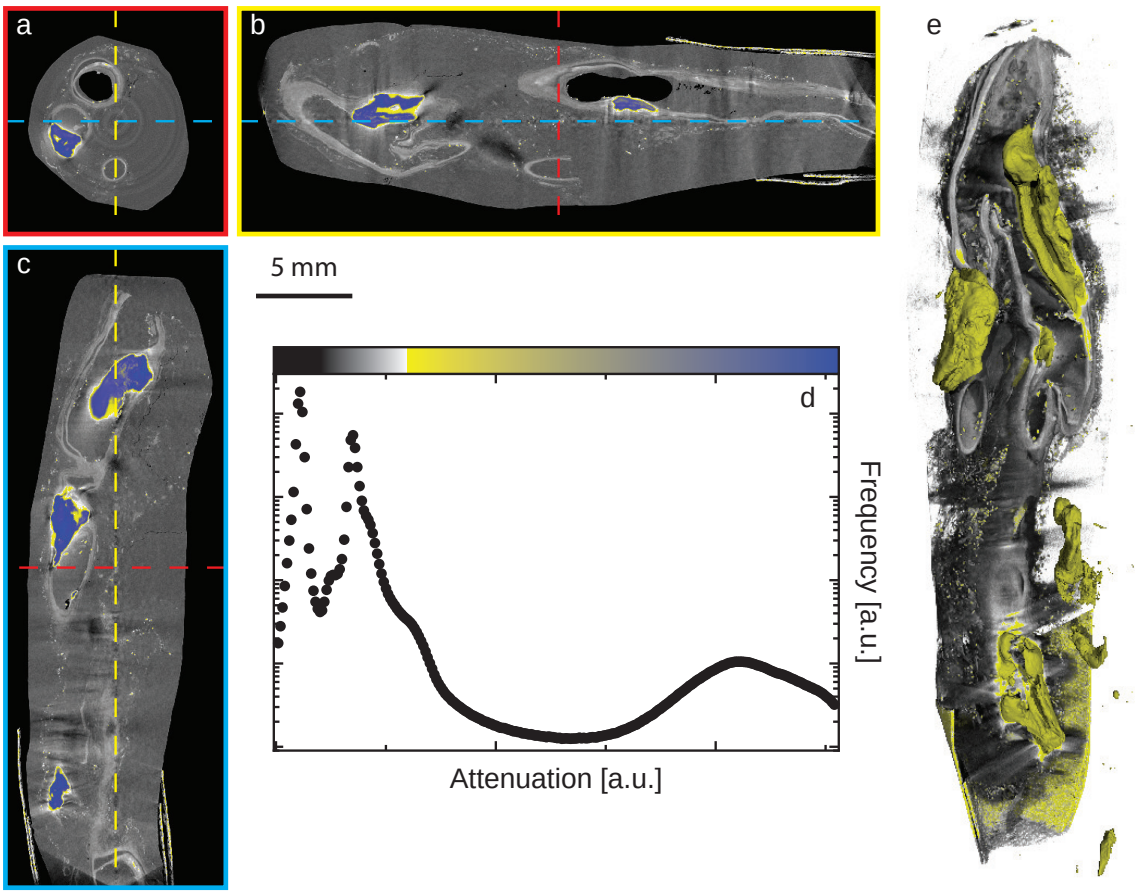

Figure 3. **(a,b,c)** Three orthogonal virtual cuts through the tomogram of a paraffin embedded stenosed coronary artery. Although the attenuation of the vessel wall (light gray) is much lower compared to that of the plaque, it can be clearly distinguished from the embedding material (dark gray). The plaque is shown in yellow to blue. **(d)** X-ray attenuation histogram with corresponding color coding. **(e)** 3D rendering of the artery. Plaque is shown in yellow, the paraffin was partially removed by thresholding.

inflammation processes or physiological bone resorption), bone grafting materials are used. This procedure has the advantage that no extensive surgery is needed, relieving patient and surgeon. The efficacy of bone grafting materials is generally assessed using histology. While well established, histology has the disadvantage of being a destructive procedure and delivering only 2D information. µCT overcomes this disadvantage by delivering full 3D morphological information non-destructively. Figures 4 a through c show three virtual orthogonal slices through the dataset of human bone biopsy extracted after insertion of bone graft (Bio-Oss®, Geistlich, Switzerland) and four months healing time, directly before implant insertion. The data were acquired at 50 kV acceleration voltage and 350 µA beam current. 1440 projections over 360° were acquired with 4 s exposure time each. The focus-specimen and focus detector distances were adjusted to 10.1 mm and 225 mm, respectively, resulting in an effective voxel length of 4.5 µm.

3.4 Distraction in rat mandible

Especially in younger patients, when cranio-facial deformities arise, correction can be performed by osteogenic distraction of the bone.[2,24] For this purpose, the bone is broken on purpose and subsequently pulled apart with a pre-defined velocity. Newly formed bone grows to fill the gap, thus augmenting total bone volume and allowing for corrections of bone shape. As bone growth velocity is limited, distraction speeds have to be adapted accordingly, meaning that intervention times are as long as weeks. To reduce discomfort to the patient, it is desirable to reduce that duration. This can be achieved by stimulating bone growth. Here, the effect of injecting

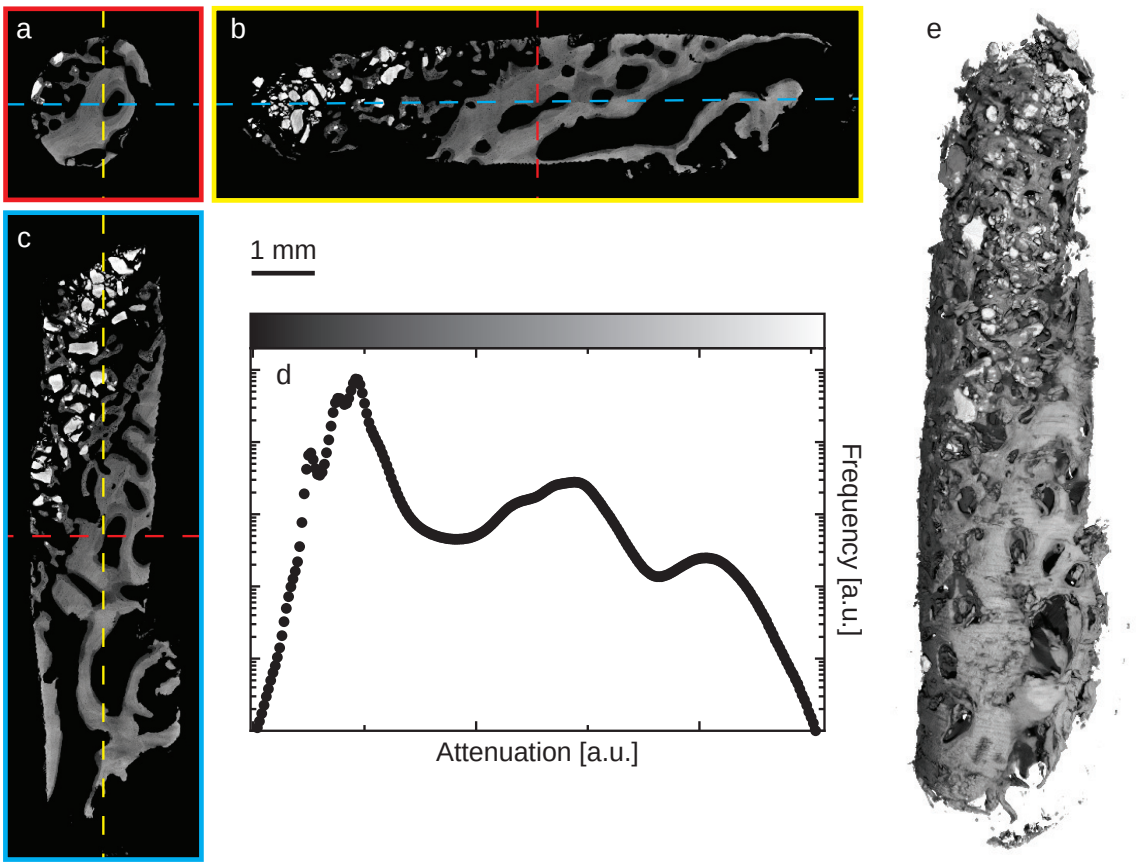

Figure 4. **(a,b,c)** Three orthogonal virtual cuts through the tomogram of a human jaw bone biopsy extracted after bone augmentation. The augmentation material appears in white to one end of the specimen, whereas the autologous bone can be seen towards the other end. Newly formed bone can be seen between the graft grains, indicating that partial osteointegration has taken place. **(d)** X-ray attenuation histogram with corresponding color coding. **(e)** 3D rendering of the biopsy. Towards the top of the specimen, the mix between graft material and newly formed bone can be seen.

human mesenchymal stem cells (hMSC) in the gap was evaluated. For this purpose, rat mandibles were distracted by 1.5 mm per day. Animals were sacrificed 66 days after distraction to allow for bone consolidation. Figure 5 a and b show, on top, the 3D rendering of two mandibles after distraction. The mandible in Fig 5a was treated with hMSC, whereas the one shown in Fig. 5b was a control. Below, virtual sections through the datasets are shown. Increased formation of new bone can be seen in Fig. 5a, while little to none can be identified in 5b. However, bone regeneration is insufficient even in the hMSC-treated jaw, indicating that distraction speed was too high. The measurements were performed on a nanotom® s operated by the Helmholz Zentrum Geesthacht outpost at the Deutsches Elektronen-Synchrotron (DESY, Hamburg Germany). 2000 projections were acquired over 360° at an acceleration voltage of 100 kV and beam current of 100 µA, at an effective pixel size of 6.9 µm. Exposure time per projection was 0.5 s.

3.5 Tooth macro-morphology

Human enamel consists of ordered hydroxyapatite crystallites organized in a fibrous continuum. Human enamel is about three times tougher than the geological counterpart and much less brittle than sintered hydroxyapatite. In the oral cavity, enamel remains functional and stable for decades under adverse mechanical and chemical conditions. One can even find millennia-old teeth. It is, therefore, the ambition of scientists to reveal the formation process and the regeneration of the anisotropic human tissues. The characteristic anatomy of the fully developed tooth reflects its formation.[25–27] For example, ameloblasts, the cells responsible for enamel formation,

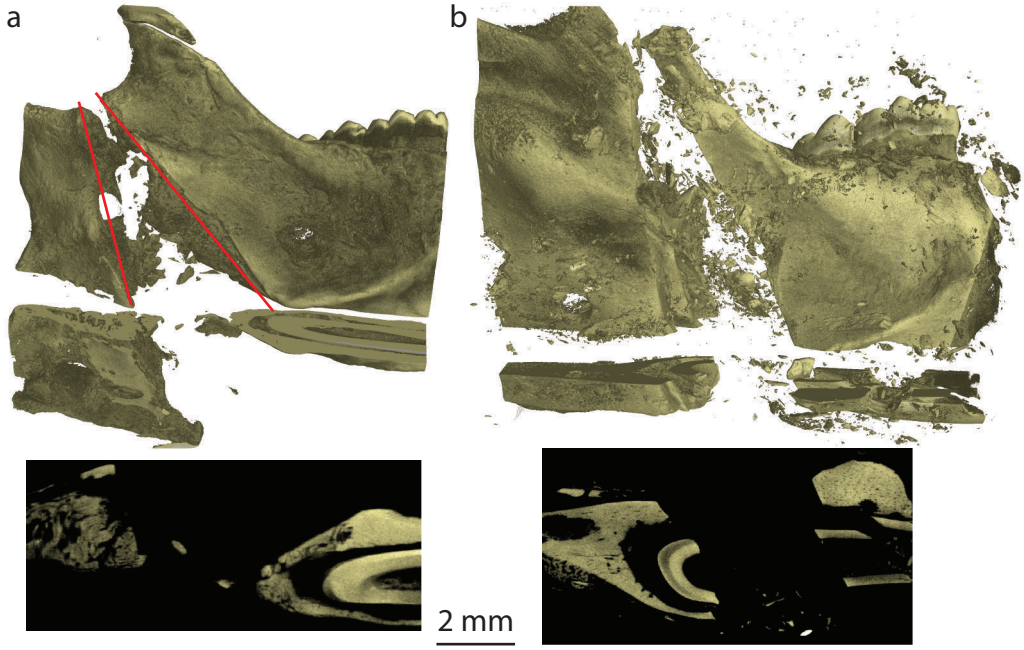

Figure 5. **(a)** Top: 3D rendering of a distracted rat mandible, seeded with human mesenchymal stem cells. Newly formed bone can be seen between the red lines. Bottom: 2D section through the dataset. Newly formed bone appears slightly darker compared to autologous bone. **(b)** Top: 2D rendering of a distracted mandible without implanted stem cells. No newly formed bone can be identified. The numerous splinters surrounding the mandible result from a specimen preparation artifact. Bottom: 2D section through the mandible, again no newly formed bone can be identified.

start at the dentin-enamel junction (DEJ) and grow outwards towards the tooth surface, depositing enamel along their paths. The DEJ itself, as stable interface between two biomaterials with distinct mechanical properties, is of high interest and matter of ongoing research,[28,29] e.g. in its role as crack propagation inhibitor.[30]
After the tooth is fully formed, ameloblasts perish, and the enamel is not actively remodeled throughout the life of the tooth. Thus, comparison of DEJ and tooth surface morphology might reveal information about how ameloblasts migrate, and allow their path during amelogenesis to be deduced. As shown in Figure 6, both tooth surface and DEJ can be extracted from µCT scans. The data shown here were acquired with a SkyScan1174^{TM} (Bruker, Belgium) tabletop scanner. Acceleration voltage was set to 50 kV and beam current to 800 µA. 900 projections were acquired over 360° with 4 s exposure time each. A 0.5 mm-thin Al filter was used to increase mean X-ray energy and reduce beam-hardening artifacts. The effective voxel length corresponded to 20.8 µm.

3.6 Tooth micro-morphology

While a minimal amount of remodeling takes place in dentin, its main macro- and micro-morphology are determined during dentinogenesis, i.e. tooth formation. In a manner analogous to enamel, the odontoblasts migrate from the DEJ to the pulp, depositing dentin. The characterizing features are the dentinal tubules, micrometer-thin channels that mark the paths of the odontodblasts.[7] As a non-destructive three-dimensional method, CT is ideally suited for their visualization. Because of the small pixel size and concurrent reduced field of view, generally only a restricted part of dentin can be visualized.[31–35] More recently, an indirect method to determine the local orientation of the dentinal tubules based on the dark-field signal from a grating interferometer was proposed.[36] However, information on individual tubules is lost. Thus, a "mosaic" approach of high-resolution scans might be desirable, and feasible given enough scan time. Figure 7a shows a virtual cut through a µCT dataset of a dentin stick some 600 µm thin, acquired with the nanotom® m at an acceleration voltage of 50 kV and a beam current of 500 µA with the W target. 1440 projections were acquired over 360°. For each projection, three frames with an exposure time of 3 s were averaged. The effective voxel length of the reconstructed data corresponds to 500 nm. Dentin tubules can be identified as dark spots. The data, however, appears noisy, and several streak

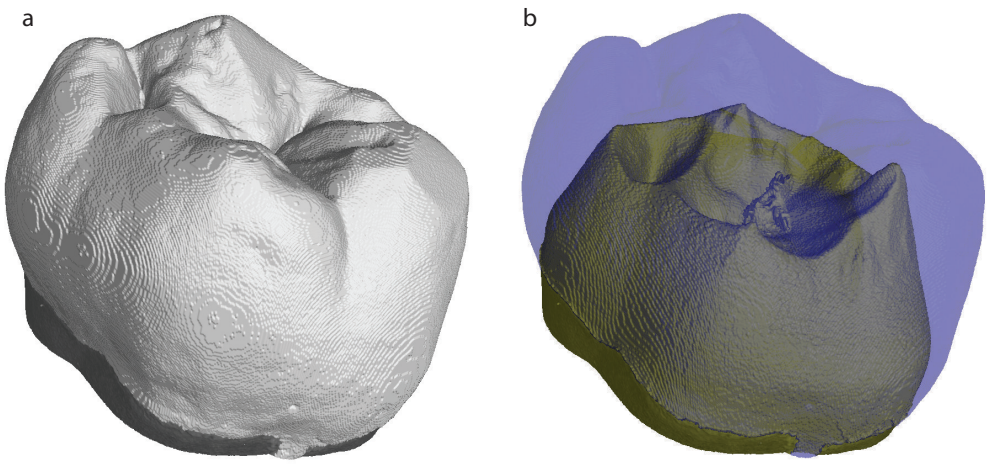

Figure 6. **(a)** 3D rendering of a human third molar crown. **(b)** Same crown, with the enamel being made transparent, the DEJ is visible. Similarities between the morphology of the enamel surface and the DEJ can be identified.

artifacts are present. Through simple data pre-processing, the quality of the tomogram can be significantly improved. Here, a 2D median filter with a kernel size of 3 pixels × 3 pixels was applied to each projection. The resulting reconstruction shows reduced noise, and streak artifacts are removed (*cf* Fig. 7b). Noise reduction, or increased contrast, is also apparent from the attenuation histogram in Fig. 7d. Peaks corresponding to air and dentin show reduced width, and the dentinal tubules give rise to a shoulder to the right of the peak related to dentin. Through this improvement, tubule segmentation becomes possible by simple thresholding, shown in Fig. 7c.

3.7 Human knee

Knee joints are load-bearing structures, subject to continuous cyclic loading. The load is transmitted to the trabecular bone, which in general has been shown to remodel to adapt to the local load.[37] Thus, a dependency of mechanical load and trabecular bone morphology exists. It is therefore of interest to monitor the morphology of trabecular bone, allowing insight to be gained into the load in healthy and diseased patients. It is advantageous to be able to image the trabecular structure within a whole knee, to compare trabecular organization over the whole joint. CT scans of specimens of these dimensions, in the order of 10 to 20 cm, are not trivial. Clinical scanners generally offer sufficient field of view (FOV), but insufficient spatial resolution, whereas µCT systems achieve sufficient resolution, but the FOV is too restricted for this kind of specimens. Figure 8 shows a 3D rendering of the µCT scan of an entire human knee acquired with the nanotom® m. Specimen diameter is just below 150 mm. The tomogram was acquired with the knee fixated and immersed in 4 % formalin solution at an acceleration voltage of 180 kV and beam current of 30 µA. Focus-specimen and focus-detector distances were adjusted to 279.5 mm and 430 mm, respectively, resulting in an effective voxel length of 65 µm. 2000 projections were acquired over 360° with 1 s exposure time each. Despite specimen size, the trabecular structure can be imaged in detail, as can be seen in Fig. 8 on the right side.

4. CONCLUSIONS

The three-dimensional visualization of specimen morphology is of interest in numerous branches of biomedical research. Micro-computed tomography provides an invaluable tool to achieve this purpose in a non-destructive way. Combined with dedicated computational tools, a wealth of information can be qualitatively and quantitatively be obtained.

ACKNOWLEDGEMENTS

The invaluable support of A. Rack during tomography experiments at ID19 (ESRF, Grenoble, France) is gratefully acknowledged. Part of the data collection was supported by Swiss National Science Foundation (SNSF)

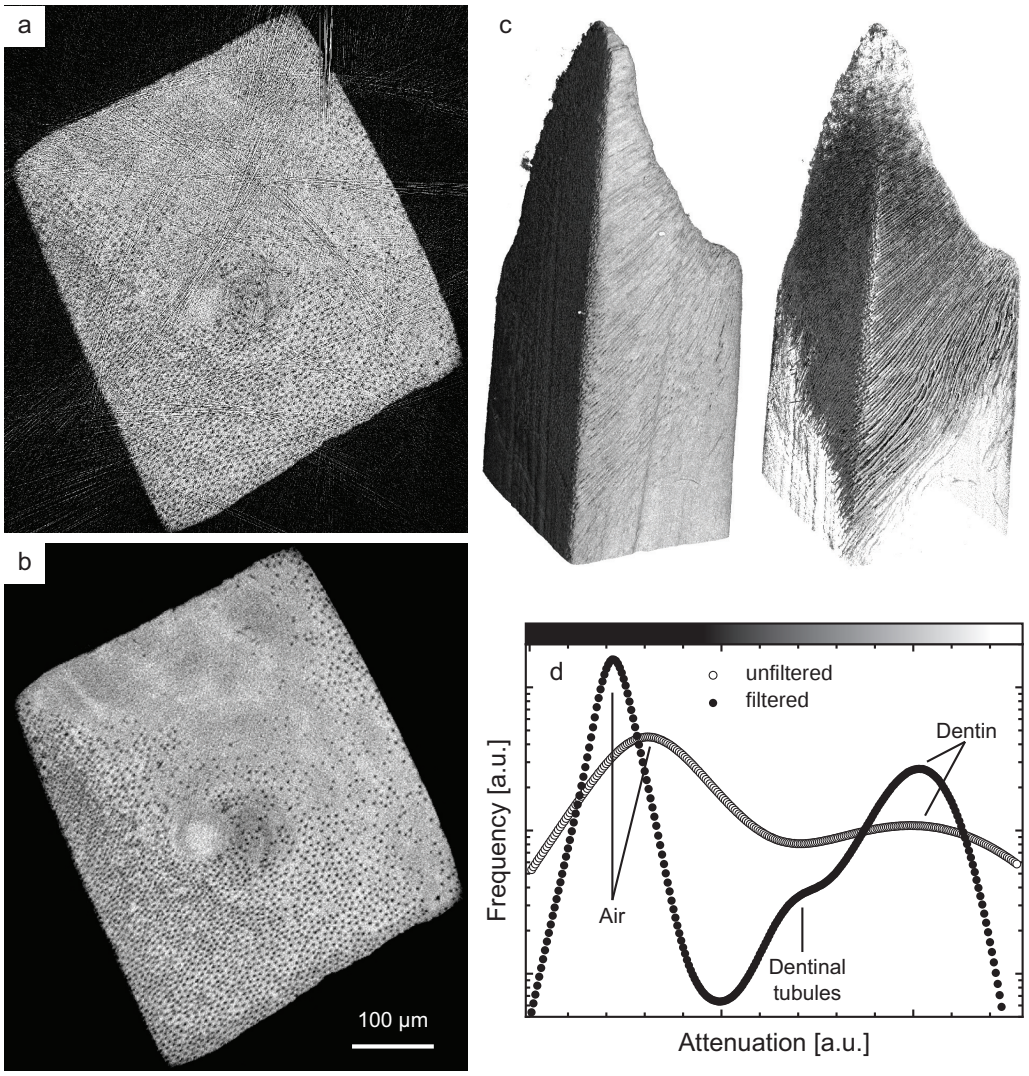

Figure 7. **(a)** Virtual section through the 3D dataset of the dentin stick, reconstructed from unfiltered projections. The data appear noisy, with several streak artifacts present. **(b)** Same virtual cut from the data reconstructed after median-filtering the projections. Filtering entirely removed streak artifacts, significantly improving data contrast. Individual tubules with a diameter of about 3.5 µm can be identified as black speckles. **(c)** 3D rendering of the dentin stick on the left, and of the segmented tubular network on the right. **(d)** Histograms of both filtered and unfiltered datasets. Peak width is significantly reduced after filtering. Also, a shoulder corresponding to the dentin tubules appears.

Figure 8. 3D rendering of a tomogram of an entire human knee with a specimen diameter of 145 mm. Despite the specimen size, the trabecular structure of the bone can be resolved.

projects 147172 and the National Research Program (NRP) 62 'Smart Materials' framework within the project number 406240_ 126090 'NO-Stress'. The authors would like to thank Nunzia Di Maggio (Tissue Engineering, University of Basel) for the preparation of the stem cells. The nanotom® m was partially funded by the SNSF R'Equip project number 316030_133802. The fruitful collaboration and exchange with Natural History Museum Basel is gratefully acknowledged.

REFERENCES

[1] Khimchenko, A., Deyhle, H., Schulz, G., Schweighauser, G., Hench, J., Chicherova, N., Bikis, C., Hieber, S. E., and Müller, B., "Extending two-dimensional histology into the third dimension through conventional micro computed tomography," *NeuroImage* **139**, 2636 (2016).

[2] Ilgenstein, B., Deyhle, H., Jaquiery, C., Kunz, C., Stalder, A., Stübinger, S., Jundt, G., Beckmann, F., Müller, B., and Hieber, S. E., "Combined micro computed tomography and histology study of bone augmentation and distraction osteogenesis," *Proc. SPIE* **8506**, 85060M (2012).

[3] Khimchenko, A., Schulz, G., Deyhle, H., Hieber, S., Hasan, S., Bikis, C., Schulz, J., Costeur, L., and Müller, B., "Non-destructive phase contrast hard x-ray imaging to reveal the three-dimensional microstructure of soft and hard tissues," *Proc. SPIE* **9797**, 97970B (2016).

[4] Müller, B., Schulz, G., Deyhle, H., Stalder, A. K., Ilgenstein, B., Holme, M. N., Weitkamp, T., Beckmann, F., and Hieber, S. E., "X-ray microscopy of soft and hard human tissues," *AIP Conf. Proc.* **1696**, 0200101–4 (2016).

[5] Buscema, M., Holme, M. N., Deyhle, H., Schulz, G., Schmitz, R., Thalmann, P., Hieber, S. E., Chicherova, N., Cattin, P. C., Beckmann, F., Herzen, J., Weitkamp, T., Saxer, T., and Müller, B., "Grating interferometry-based phase microtomography of atherosclerotic human arteries," *Proc. SPIE* **9212**, 921203 (2014).

[6] Lang, S., Zanette, I., Dominietto, M., Langer, M., Rack, A., Schulz, G., Duc, G. L., David, C., Mohr, J., Pfeiffer, F., Müller, B., and Weitkamp, T., "Experimental comparison of grating- and propagation-based hard x-ray phase tomography of soft tissue," *J. Appl. Phys.* **116**, 154903 (2014).

[7] Deyhle, H., Weitkamp, T., Lang, S., Schulz, G., Rack, A., Zanette, I., and Müller, B., "Comparison of propagation-based phase-contrast tomography approaches for the evaluation of dentin microstructure," *Proc. SPIE* **8506**, 85060N (2012).

[8] Weitkamp, T., Diaz, A., David, C., Pfeiffer, F., Stampanoni, M., Cloetens, P., and Ziegler, E., "X-ray phase imaging with a grating interferometer," *Opt. Express* **13**, 6296–6304 (2005).

[9] Momose, A., Kawamoto, S., Koyama, I., Hamaishi, Y., Takai, H., and Suzuki, Y., "Demonstration of x-ray talbot interferometry," *Jpn. J. Appl. Phys.* **42**, L866 (2003).

[10] Cloetens, P., Barrett, R., Baruchel, J., Guigay, J.-P., and Schlenker, M., "Phase objects in synchrotron radiation hard x-ray imaging," *J. Phys. D Appl. Phys.* **29**, 133–146 (1996).

[11] Rodenburg, M., Hurst, A. C., Cullis, A. G., Dobson, B. R., Pfeiffer, F., Bunk, O., David, C., Jefimovs, K., and Johnson, I., "Hard-x-ray lensless imaging of extended objects," *Phys. Rev. Lett.* **98**, 034801 (2007).

[12] Thibault, P., Dierolf, M., Menzel, A., Bunk, O., David, C., and Pfeiffer, F., "High-resolution scanning x-ray diffraction microscopy," *Science* **321**, 379–382 (2008).

[13] Stockmar, M., Cloetens, P., Zanette, I., Enders, B., Dierolf, M., Pfeiffer, F., and Thibault, P., "Near-field ptychography: phase retrieval for inline holography using a structured illumination," *Sci. Rep.* **3**, 1927 (2013).

[14] Holler, M., Diaz, A., Guizar-Sicairos, M., Karvinen, P., Färm, E., Härkönen, E., Ritala, M., Menzel, A., Raabe, J., and Bunk, O., "X-ray ptychographic computed tomography at 16 nm isotropic 3d resolution," *Sci. Rep.* **4**, 3857 (2014).

[15] Brunke, O., Brockdorf, K., Santillan, J., Drews, S., Müller, B., Donath, T., Herzen, J., and Beckmann, F., "Comparison between x-ray tube based and synchrotron radiation based μct," *Proc. SPIE* **7078**, 70780U (2008).

[16] Müller, B., Beckmann, F., Huser, M., Maspero, F., Szekely, G., Ruffieux, K., Thurner, P., and Wintermantel, E., "Non-destructive three-dimensional evaluation of a polymer sponge by micro-tomography using synchrotron radiation," *Biomol. Eng.* **19**, 73–78 (2002).

[17] Stalder, A., Ilgenstein, B., Chicerova, N., Deyhle, H., Beckmann, F., Müller, B., and Hieber, S. E., "Combined use of micro computed tomography and histology to evaluate the regenerative capacity of bone grafting materials," *Int. J. Mater. Res.* **105**, 679–691 (2014).

[18] Hieber, S. E., Bikis, C., Khimchenko, A., Schweighauser, G., Hench, J., Chicherova, N., Schulz, G., and Müller, B., "Tomographic brain imaging with nucleolar detail and automatic cell counting," *Sci. Rep.* **6**, 32156 (2016).

[19] Weitkamp, T., Zanette, I., David, C., Baruchel, J., Bech, M., Bernard, P., Deyhle, H., Donath, T., Kenntner, J., Lang, S., Mohr, J., Müller, B., Pfeiffer, F., Reznikova, E., Rutishauser, S., Schulz, G., Tapfer, A., and Valade, J., "Recent developments in x-ray talbot interferometry at esrf-id19," *Proc. SPIE* **7804**, 780406 (2010).

[20] WHO, "Fact sheet n. 310]," *www.who.int* (May 2014).

[21] Holme, M. N., Fedotenko, I. A., Abegg, D., Althaus, J., Babel, L., Favarger, F., Reiter, R., Tanasescu, R., Zaffalon, P.-L., Ziegler, A., Müller, B., Saxer, T., and Zumbuehl, A., "Shear-stress sensitive lenticular vesicles for targeted drug delivery," *Nature Nanotech.* **7**, 536–543 (2012).

[22] Holme, M. N., Schulz, G., Deyhle, H., Weitkamp, T., Beckmann, F., Lobrinus, J. A., Rikhtegar, F., Kurtcuoglu, V., Zanette, I., Saxer, T., and Müller, B., "Complementary x-ray tomography techniques for histology-validated 3d imaging of soft and hard human tissues using plaque-containing blood vessels as examples," *Nat. Prot.* **9**, 14011415 (2014).

[23] Buscema, M., Deyhle, H., Pfohl, T., Hieber, S., Zumbuehl, A., and Müller, B., "Characterization of mechano-sensitive nano-containers for targeted vasodilation," *Proc. SPIE* **9797**, 97970S (2016).

[24] Hieber, S. E., Müller, B., Jaquiery, C., and Kunz, C., "Mikrotomographische analyse der knochendistraktion," *Swiss Med. Forum* **13**, 612–613 (2013).

[25] Deyhle, H., Bunk, O., Buser, S., Krastl, G., Zitzmann, N., Ilgenstein, B., Beckmann, F., Pfeiffer, F., Weiger, R., and Müller, B., "Bio-inspired dental fillings," *Proc. SPIE* **7401**, 74010E (2009).

[26] Gaiser, S., Deyhle, H., Bunk, O., White, S., and Müller, B., "Understanding nano-anatomy of healthy and carious human teeth: a prerequisite for nanodentistry," *Biointerphases* **7**, 4 (2012).

[27] Deyhle, H., White, S. N., Bunk, O., Beckmann, F., and Müller, B., "Nanostructure of the carious tooth enamel lesion," *Acta Biomater.* **10**, 355–364 (2014).

[28] Stock, S. R., Vieira, A. E. M., Delbem, A. C. B., Cannon, M. L., Xiao, X., and Carlo, F. D., "Synchrotron microcomputed tomography of the mature bovine dentinoenamel junction," *J. Struct. Biol.* **161**, 162–171 (2008).

[29] Sui, T., Lunt, A. J. G., Baimpas, N., Sandholzer, M. A., Li, T., Zeng, K., Landini, G., and Korsunsky, A. M., "Understanding natures residual strain engineering at the human dentineenamel junction interface," *Acta Biomater.* **32**, 256–263 (2016).

[30] Imbeni, V., Kruzic, J. J., Marshall, G. W., Marshall, S. J., and Ritchie, R. O., "The dentinenamel junction and the fracture of human teeth," *Nature Mater.* **4**, 229–232 (2005).

[31] Zabler, S., Riesemeier, H., Fratzl, P., and Zaslansky, P., "Fresnel-propagated imaging for the study of human tooth dentin by partially coherent x-ray tomography," *Opt. Express* **14**, 85848597 (2006).

[32] Zabler, S., Cloetens, P., and Zaslansky, P., "Fresnel-propagated submicrometer x-ray imaging of waterimmersed tooth dentin," *Opt. Lett.* **32**, 29872989 (2007).

[33] Zaslansky, P., Zabler, S., and Fratzl, P., "3d variations in human crown dentin tubule orientation: A phase-contrast microtomography study," *Dent. Mater.* **26**, e1e10 (2010).

[34] Parkinson, C. R. and Sasov, A., "High-resolution non-destructive 3d interrogation of dentin using x-ray nanotomography," *Dent. Mater.* **24**, 773777 (2008).

[35] Zanette, I., Enders, B., Dierolf, M., Thibault, P., Gradl, R., Diaz, A., Guizar-Sicairos, M., Menzel, A., Pfeiffer, F., and Zaslansky, P., "Ptychographic x-ray nanotomography quantifies mineral distributions in human dentine," *Sci. Rep.* **5**, 9210 (2015).

[36] Jud, C., Schaff, F., Zanette, I., Wolf, J., Fehringer, A., and Pfeiffer, F., "Dentinal tubules revealed with x-ray tensor tomography," *Dent. Mater.* **32**, 1189–1195 (2016).

[37] Hoechel, S., Schulz, G., and Müller-Gerbl, M., "Insight into the 3d-trabecular architecture of the human patella," *Annals Anat.* **200**, 98104 (2015).